Highly active Fe-N-reduced graphene oxide electrocatalysts using sustainable amino acids as nitrogen source

Heresh Rayej[1], Mohammad Reza Vaezi[1], Behzad Aghabarari[1], Ramiro Ruiz-Rosas[2], Juana Mª Rosas[2], José Rodríguez-Mirasol[2,*], Tomás Cordero[2]

1- Department of Nanotechnology and Advanced Material, Materials and Energy Research Center (MERC), Alborz, 31787-316, Iran

2 - Universidad de Málaga, Andalucia Tech., Departamento de Ingeniería química, Campus de Teatinos s/n, 29010, Málaga, Spain

*: Corresponding author. Email address: mirasol@uma.es, phone number: +34951952385

Abstract

This work reports the preparation of oxygen reduction reaction catalysts by pyrolysis of a mixture of $Fe(NO_3)_3$ and graphene oxide (GO) functionalized with three different amino acids, Arginine (Arg), Cysteine (Cys), Histidine (His). The combination of TPD, FTIR and XPS revealed that the functionalization of GO rendered a reduction of epoxide and carboxyl surface groups at along with the preferential generation of amide bridges. XPS confirmed the incorporation of nitrogen in edge and quaternary positions of the graphene layers after the pyrolysis at 800 ºC of the amino acid functionalized GO mainly in form of pyridines (Arg), pyrroles (Cys) and quaternary nitrogen (His). XRD and XPS showed that most iron is retained after pyrolysis in the form of crystalline Fe_3O_4 and in a lesser extend as Fe_2O_3. The amount, distribution, and particle size of iron species on the pyrolyzed samples relies on the amino acid used for the modification, with histidine rendering the lower retained amount and higher dispersion. Raman analyses pointed out that the structural order seems to follow the order His>Cys>Arg. The electrochemical characterization revealed that, in spite of having a lower iron content, Fe-rGO-His shows a higher double layer capacitance, improved conductivity and enhanced ORR activity than their counterparts, delivering onset and half-wave potentials only 30 mV behind the current state-of-the-art platinum-carbon black catalyst. These results confirm that amino acids, and specially Histidine, can be interesting N-dopant agents for the preparation of nitrogen-iron graphene electrocatalysts with excellent ORR activities.

***Keywords**:* Oxygen reduction reaction, Amino acids, Graphene, nitrogen doping, iron

1. Introduction.

Over the past decade, a strong research effort has been focused on the Oxygen reduction reaction (ORR). ORR is undeniably at the core of energy storage and conversion systems, such as metal-air batteries and fuel cells fuel. However, the industrial development of energy conversion systems has been hindered by the high cost of platinum, which is the metal of choice for the production ORR electro catalysts owing to its outstanding activity. In this sense, the scarcity and high costs, due to its limited reserves and the increasing demand in the market, along with several performance issues, such as the activity decline by low stability or under fuel crossover scenarios, greatly hampers the commercial success of energy devices based on ORR. To date many efforts have been made to overcome these problems, such as decreasing the platinum loading by the production of nanoparticles and/or alloys, or replacement of platinum by transition metals or even metal free carbon-based catalyst[1-4].

Today, Graphene (GR) has stood in the spotlight of research related to materials science, physics, chemistry, and nanotechnology. Ideally, GR is a two-dimensional carbon structure as thick as an atom that has a honeycomb-like structure[5]. However, several nanostructured carbon materials sharing a similar structure but with different degrees of structural order and surface chemistry composition are also regarded as graphene, like exfoliated graphite by mechanical methods, few-layered graphene by chemical vapor deposition or reduced graphene oxide [6]. GR properties relies on the preparation method. For instance, exfoliated graphite shows extraordinary properties, such as excellent thermal and electrical conductivity, high optical transparency, high surface area and Young modulus [7-10], but massive GR production is not achievable following this procedure.

In this sense, the chemical-thermal reduction of graphene oxide (GO) can be highlighted as one of the most viable production pathways. Graphene oxide has a hexagonal structure resembling the one of GR, but it contains a large number of surface oxygen groups, such as epoxides, hydroxyls and carboxylic acid moieties [11]. The most common method of producing GO is the Hummers chemical method [12, 13], consisting of the oxidation of graphite using protonated solvents, which delivers the formation of graphite oxide. The basic unit structure of Graphite oxide is GO, and therefore GO can be obtained by delamination of graphite oxide using mechanical methods. The presence of oxygen groups in GO has benefits and drawbacks. They increase the solubility and processability of GO compared to GR and enables a wide number of functionalization routes. However, they also neglect some of the unique GR properties, such as electrical conductivity. The functional groups of GO are removed by reduction, generating reduced graphene oxide (rGO), which is a family member of GR materials [14]. There are a large number of methods available for reducing GO to produce Gr or rGO, from where thermal or chemical reduction are the most widely used due to their ease.

Among these methods, the treatment with amino acids (AAs) have been used not only to reduce GO but also to functionalize Gr and GO, and even to produce Gr through graphite exfoliation by AA intercalation[15]. In this regard, Chwalibog *et al*. achieved significant and positive results in their research work on Gr functionalized with arginine for the treatment of glioblastoma multiform [16]. In another research work, Shabani *et al*. studied the reduction and functionalization of GO by the L-histidine amino acid [17]. Moreover, the production of N-doped carbon materials as sustainable ORR electro catalysts via AA functionalization of GO have been proposed using cysteine and arginine [18-21].

77 Interestingly, the activity of N-doped carbon materials for ORR increases when combined
78 with transition metals, showing high activity, high selectivity to water and strong resistance to
79 poisoning and fuel crossover [22]. Between them, the Fe-N pair have been proposed as an
80 outstanding active site for ORR, being the most promising alternative to platinum in terms of
81 availability, cost and activity [23]. Synthesis of Fe-N catalysts usually follow two different
82 pathways, namely i) loading of iron nanoparticles or iron precursor on top of N-doped carbon
83 materials followed by thermal reduction [24] and ii) pyrolysis of iron and nitrogen-rich
84 precursors on the surface of carbon materials [25]. To the date, there are only a few works
85 dealing with the preparation of Fe-N ORR catalysts using amino acids [26, 27]. However, to our
86 knowledge, there is no report concerning the use of different amino acids for GO
87 functionalization and subsequent production of Fe-N-rGO catalysts by thermal treatment in the
88 presence of iron precursor. This synthesis could be a sustainable approach to produce
89 nanostructured rGO catalysts for the oxygen reduction reaction [27-31].
90 In this work, iron loaded N-doped reduced graphene oxide were prepared by functionalization
91 of GO using three different amino acids, cysteine, histidine, and arginine followed by pyrolysis
92 in the presence of iron nitrate. The porosity, surface chemistry and structure of the resulting
93 materials have been characterized, and their activity towards ORR in acid and alkaline
94 electrolyte has been evaluated.
95

2. Materials and Methods

2.1. Synthesis of electrocatalysts

GO was first synthesized through Hummers method [10]. Briefly, natural graphite flakes (Asbury Graphite Mills, US) and sulfuric acid (H_2SO_4, 95.5–96.5%) were mixed and stirred at 200 rpm. Fuming nitric acid (HNO_3, 65%) was added into the mixture and stirred for 24 h at room temperature. Then, deionized water was added slowly, and the obtained mixture was washed and dried at 60 °C to obtain graphite intercalation compounds (GIC). To obtain Expanded Graphite (EG), the dry GIC powder was thermally expanded at 1050° C for 15 s. EG maintains the graphite layered structure, but the interlayer space can expand to more than 150 times. Therefore, oxidizing agents for the preparation of GO will diffuse faster between the layers of expanded graphite. Then, 1 g of EG and 200 ml of sulfuric acid were mixed and stirred. After that, 10 g of $KMnO_4$ was added dropwise. The obtained mixture was transferred into an ice bath and 200 ml of deionized water (DW) and 50 ml of H_2O_2 was added, the color of the mixture changed to light brown. The GO particles were stirred, washed with HCl later centrifuged.

Arginine, cysteine and histidine were selected for GO functionalization because of their high content of N in arginine (Arg), the presence of both N and S in cysteine (Cys), and the presence of imidazole group and N in histidine structure (His). A GO:AA ratio of 1:2 was selected for GO:AA [32-34]. The details of the synthesis of catalysts are as follow: first, 80 mL of GO solution containing 100 mg of dissolved GO was placed on a stirrer. 200 mg of the amino acids were dissolved in 10 mL of DW separately in a beaker and later added to the GO solution. The GO-AA solution was placed on a stirrer for 8 hours at room temperature (25 °C). For recovering the solids, the solutions were centrifuged at 18000 rpm for 10 minutes (This action was repeated three times), filtered using a nylon membrane (pore size 430 nm, Millipore) and dried at 80 ºC.

The GO-AA solids were recovered at this point in the form of brittle flakes and stored for further characterization. These samples have been named as GO-Arg, GO-Cys and GO-His in accordance with the amino acid employed during the functionalization.

For the preparation of the Fe-N-rGO catalysts, GO-AA samples served as support, whereas Fe $(NO_3)_3 \cdot 9H_2O$ was chosen as the iron source. A solution of Fe $(NO_3)_3$ (0.1 M) in distilled water was added to GO-AA solutions containing the different amino acids (GO:AA: $Fe(NO_3)_3 \cdot 9H_2O$ ratio of 1:2:0.66) and mixed on a stirrer at room temperature for 24 hours. The resulting solution was then centrifuged at 18000 rpm for 10 minutes to remove the excess of water. The recovered wet solid was then placed in an alumina crucible, dried at 50 ºC overnight and heated up inside a furnace at 800 °C (heating rate: 10 ºC/min, holding time: 10 minutes) under N_2 atmosphere (flow rate: 150 mL/min STP) to pyrolyze the mixture and obtain Fe-N-C catalysts [35]. The final solids have been named as Fe-rGO-Arg, Fe-rGO-Cys and Fe-rGO-His, depending on the amino acid used in the functionalization step. For comparison purposes, iron-free GO-AA samples were also pyrolyzed at 800 ºC under the previously described conditions to obtained reduced graphene oxide samples, labelled as rGO-AA.

2.3. Characterization

In this study, the elemental composition of the samples was analyzed in a TruSpec micro CHNSO (Leco) to determine the mass fractions of carbon, hydrogen, nitrogen and sulfur. The surface chemistry of the samples was analyzed through X-ray photoelectron spectroscopy (PHI 5000 VersaProbe II model, Physical Electronics) with monochromatic Al k-alpha radiation, beam being focused in a 10-micrometer window. The whole spectrum was shifted using as reference the position of the C1s peak, which was set to 284.5 eV. Fourier-transform infrared spectroscopy (FTIR, SHIMADZU, 8400S model) was used to check the formation of functional

groups in the structure of GO and the doping of the desired metal. The amount and type of oxygen surface groups were analyzed by Temperature Programmed Desorption (TPD), which was performed in a custom quartz reactor by heating 15-30 mg of GO and GO-AA samples from room temperature up to 900 ºC under N_2 flow (150 mL/min STP) using a heating rate of 10 ºC/min. The desorption rate of CO and CO_2 during this thermal run was measured using NDIR detectors (Ultramat 23, Siemens). Furthermore, X-ray diffraction patterns (XRD) of the samples were recorded using a 2θ range between 5 and 90° in an EMPYREAN diffractometer (PANalytical), using CuKα monochromatic radiation operating at 45 kV and 40 mA. Raman spectra of the samples were registered in an Invia Qontor Raman Confocal microscope (RENISHAW), using the 532 nm laser line (grating: 240 L/mm, slit opening of 50 μm) and a spectral resolution of ±1 cm^{-1}. The power of the beam was set to 0.27 mW to avoid any modification of the samples during the measurement. The morphology of the samples was studied by transmission electron microscopy (TEM) images with a JEOL JEM-2010 microscope operated at 200 kV. In addition to the above diagnostic analyses, electrochemical characterization and activity tests related to ORR were performed.

2.4. Electrochemical test

The electrochemical characterization of the samples was carried out using an SP-200 potentiostat (biologic) in 3-electrode cell configuration, where a graphite rod and saturated calomel electrode (SCE) were set as counter and reference electrode, respectively. The working electrode consisted in a rotating disk electrode (RDE, OrigaTrod, Origalis) made of glassy carbon (GC, 5 mm diameter). For the preparation of the working electrode assembly, 1 mg/mL ink is prepared by mixing 5 mg of the sample with 5 mL of a solution consisting in 5:1:0.5 water:isopropanol:Nafion© (5% solution, Sigma Aldrich). The mixture is sonicated in ultrasound

bath for 20 minutes. The GC electrode was then decorated with the sample by pipetting 20 μL of the ink on top of the GC surface (electrode loading of ca. 100 μg/cm) and drying the GC at 110 ºC.

ORR electrochemical activity tests were carried out at 25 °C in alkali electrolyte (0.1 M KOH). The electrochemical behavior of the working electrode was analyzed by performing 20 cyclic voltammetry (CV) cycles at 50 mV/s in the 0 to 1.2 V vs reversible hydrogen electrode (RHE) range using N_2-saturated electrolyte. CV and linear sweep voltammetry (LSV) from 0 to 1 V were performed at 5 mV/s in N_2 and O_2-saturated electrolyte and under different rotating rates (from 400 to 2025 rpm). The number of electrons transferred during ORR, *n*, were determined using the Kouteky Levich (KL) equation, for which the following equation was used:

$$\frac{1}{j} = \frac{1}{j_K} + \frac{1}{J_L} = \frac{1}{j_K} + \frac{1}{B \cdot n} \cdot w^{-1/2}$$

where j_K and j_L are the kinetic and mass transfer limited current densities, j is the experimentally observed current density, w is the angular velocity and B is the proportionality coefficient, which can be calculated as:

$$B = 0.62 \cdot D_{O2}^{2/3} \cdot C_{O2} \cdot v^{-1/6} \cdot F$$

In this equation, D_{O2} is the diffusion coefficient of oxygen, C_{O2} is the bulk concentration of O_2, v is the kinematic viscosity of the electrolyte and F is the Faraday constant.

The electrochemical response and ORR activity of commercial 20% platinum on Vulcan XC72 catalyst (Sigma-Aldrich) was also analyzed using the same protocol for comparison purposes.

3. Results and discussion

3.1. GO functionalization with amino acids

The composition of GO before and after functionalization with AA was determined by ultimate analyses, Table 1. GO was dried at 60 ºC under vacuum prior for this measurement. The analyses confirm the presence of nitrogen in all GO-AA samples due to the successful linking of the biomolecules on the surface of graphene oxide. The loss of oxygen is an interesting side result that could be related to the chemical reduction of GO amino acids [15]. The presence of sulfur in GO-Cys is a desired feature of this sample and comes from the presence of thiol group in cysteine. Considering the amounts of nitrogen in the parent AAs and the absence of nitrogen in GO, the maximum theoretical nitrogen loading that can be achieved at 1:2 GO:AA for each sample would be 32.1, 11.6 and 27.1 N wt.% for GO-Arg, GO-Cys and GO-His, respectively. Considering the nitrogen amounts detected by ultimate analyses (Table 1), the estimated N fixation ratios were 38, 30 and 34 % for GO-Arg, GO-Cys and GO-His, respectively. The slightly higher incorporation of N by arginine fixation is probably due to the presence of terminal amino functions, which could form amide bridges with carboxylic moieties of GO [36]. It is also important to note that the cysteine molecule has a N:S atomic ratio of 1:1, whereas the elemental analysis of GO-Cys sample showed an experimental ratio of 2:1, which could be related to the loss of the thiol group due to the partial decomposition of the AA after functionalization.

Table 1. Elemental composition of samples (%, dry & ash free basis)

Sample	C		H		N		S		O*	
	wt[#]	*at*[$]	*wt*	*at*	*wt*	*at*	*wt*	*at*	*wt*	*at*
GO	42.4	38.8	2.1	23.1	0.0	0.0	0.0	0.0	55.5	38.1
GO-ARG	54.2	38.6	4.5	38.4	12.3	7.5	0.1	0.0	28.9	15.4
GO-CYS	55.7	42.7	3.8	34.9	3.5	2.3	4.0	1.1	33.0	19.0
GO-HIS	51.4	41.2	3.2	30.8	9.1	6.3	0.1	0.0	36.1	21.7
rGO-ARG	79.9	69.7	1.7	17.8	4.9	3.7	0.0	0.0	13.5	8.8
rGO-CYS	82.7	76.0	1.2	13.2	2.6	2.0	1.8	0.6	11.7	8.1
rGO-HIS	83.2	74.3	1.4	15.0	3.8	2.9	0.0	0.0	11.6	7.8
Fe-rGO-ARG	89.2	78.7	1.4	14.8	2.4	1.8	0.0	0.0	7.0	4.6
Fe-rGO-CYS	90.7	81.0	1.3	13.9	2.0	1.5	1.4	0.5	4.6	3.1
Fe-rGO-HIS	90.6	79.8	1.4	14.8	1.3	1.0	0.0	0.0	6.7	4.4

*O= 100 -C -H -N -S – ash

#wt= weight concentration

$at= atomic concentration

FTIR spectra of GO and GO-AA samples were recorded and are compiled in Fig. 1. It can be seen that GO shows as its main features the absorption bands related to the presence of carboxyl groups at 1735 cm^{-1}, as well as the C-O stretching vibration from epoxy groups at 1060 cm^{-1} and the broad band at 3250 cm^{-1} owing to the presence of hydroxyl functionalities. After functionalization with amino acids, (GO-His, GO-Cys and GO-Arg in Figure 1), new bands emerge in GO-AA samples related to the presence of the respective amino acids, such as the

stretching vibration of C-N at 1610 cm^{-1} and 1335 cm^{-1} for histidine. Less significant peaks related to the different bonds of each amino acid are also observed.

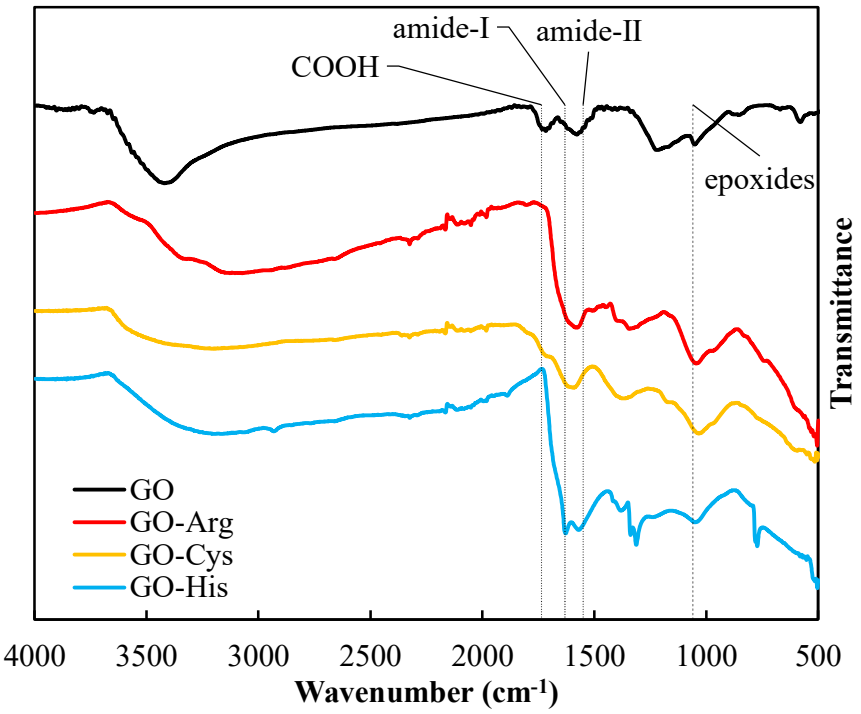

Figure 1. FT-IR spectra of GO, GO-Arg, GO-His and GO-Cys samples.

Interestingly, these spectra also confirm the formation of amide bridges through the development of amide-I and amide-II bands at around 1630 and 1550 cm^{-1}, respectively [37], being especially clear for GO-His. In line with this, a strong decrease in the bands related to the carboxyl type functional groups is observed at 1735 cm^{-1}, suggesting that the main functionalization pathway of GO with the involved amino acids proceeds through the formation of amide bridges via the reaction of the amine groups with GO carboxylic acid groups. The FTIR spectra of all the samples also reveals that the peak related to epoxy groups is severely modified, showing the contribution of C-O vibrations from the functional groups of the amino acids. In this line, others authors have also reported the reduction of GO using amino acids [38]. Specifically, Tran et al.

observed the loss of hydroxyl, carbonyl and epoxy groups during the deoxygenation of GO using aspartic acid and valine [39].

The CO and CO_2 temperature programmed desorption (TPD) profiles of GO, GO-cys, GO-Arg and GO-His were measured to study the thermal reduction of GO before and after the amino acid functionalization of these samples. For the sake of comparison, thermal decomposition of pure cysteine, arginine and histidine was also analyzed. TPD is a technique that allows to identify the surface oxygen groups in carbon materials attending to their different thermal stability and the formation of either CO or CO_2 [40].

Figure 2.a and 2.b compares the CO and CO_2 profiles, respectively, of GO before and after the functionalization with histidine and arginine. Cysteine functionalization showed similar profiles than GO-His and was not included for the sake of clarity. The TPD profiles of pristine GO shows high evolution of CO and CO_2 at ca. 100 ºC in a narrow interval of temperatures, which is related to the presence of large quantities of labile and rather unstable epoxy and hydroxyl groups in the basal plane [41, 42]. The CO_2 evolution in the range of 200-300 ºC is ascribed to the presence of carboxyl groups at edge sites, as reported for conventional carbon materials [40]. Between 400 and 600 ºC, the CO and CO_2 evolution rates of GO grow in parallel due to the thermal decomposition of anhydrides. Beyond temperatures of 600 ºC, CO release still increases due to the decomposition of phenol and carbonyl groups at edge positions [40].

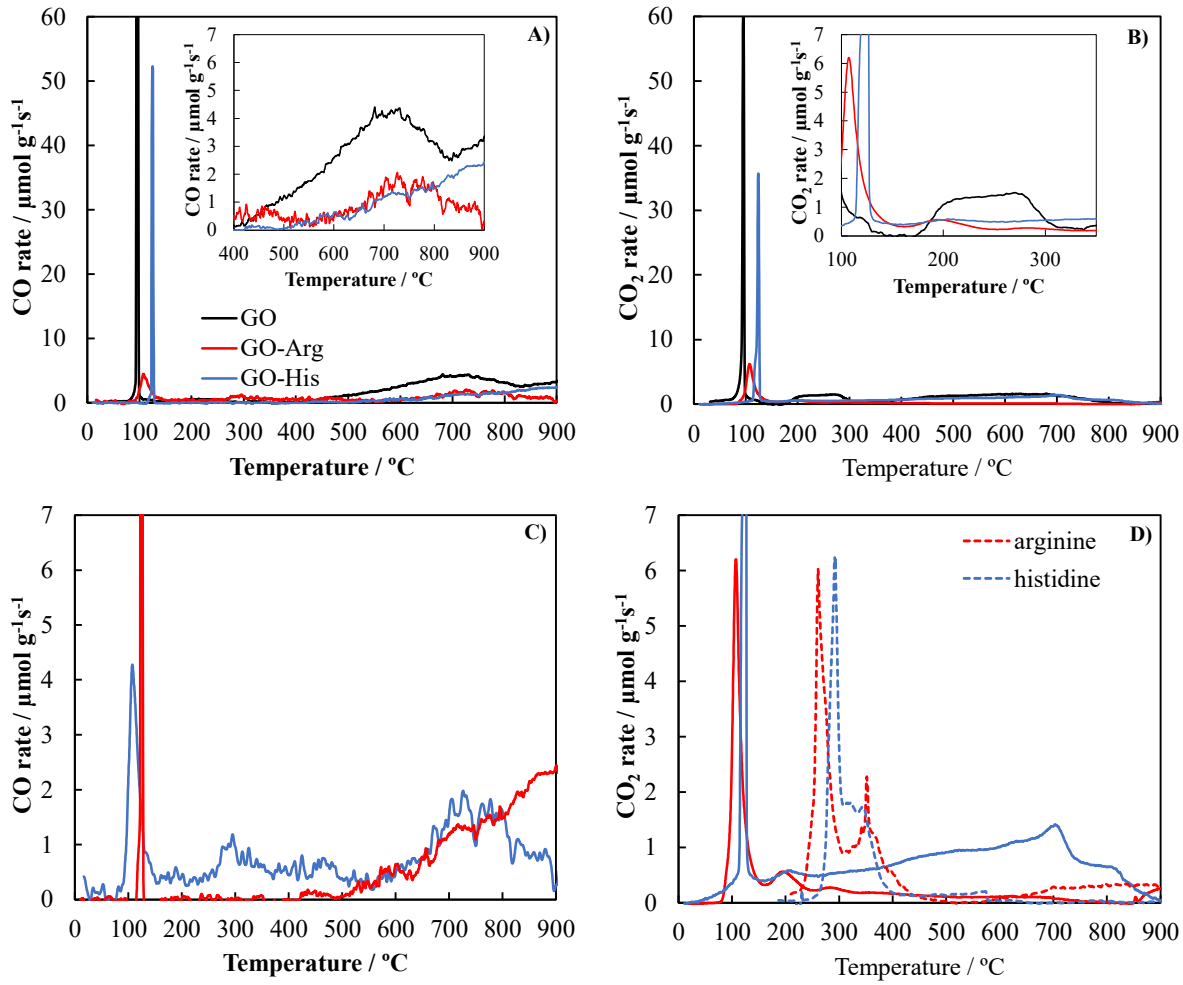

Figure 2. A) CO- and B) CO_2-Temperature Programmed Desorption profiles of GO, GO-Arg and GO-His. C) detailed CO-TPD and D) CO_2-TPD profile of GO-Arg and GO-His, and the parent amino acids (dotted lines)

Table 2. CO and CO_2 evolution and oxygen content determined from TPD analyses

Sample	CO mMol / g	CO_2 mMol / g	Total O mMol / g	Total O wt. %
GO	12.35	5.86	21.45	38.5
GO-Cys	3.65	3.25	10.15	16.2
GO-Arg	3.50	1.48	6.45	10.3
GO-His	3.78	4.39	12.56	20.1

252

253 Table 2 compiles the amount of CO and CO_2 evolved from GO before and after functionalization
254 with amino acids. The total amount of oxygen measured from this technique is lower than the
255 values obtained from ultimate analyses due to the presence of interstitial water in GO (which is
256 known to be the main released product at temperatures around 100 – 150 ºC [41, 43]), water
257 coordinated with carboxylic functionalities and probably surface oxygen groups of large thermal
258 stability that remains on the carbon surface even at temperatures higher than 900 ºC, such as
259 pyrone groups [44].

260 After functionalization, a strong decrease in the low temperature CO and CO_2 evolution peaks,
261 along with a temperature shift to higher values is observed. In addition, the carboxylic moieties
262 of GO at temperatures between 200 and 300 ºC are lost, inset of Fig. 2.b, which seems to confirm
263 the FTIR results regarding preferential functionalization of amino acids via formation of amide
264 bridges. It is also important to note that AA functionalization produce a decrease in the CO
265 evolution in the range of 500 to 800 ºC, inset of Fig. 2.a, which is likely related to side reactions
266 between the amino acids and hydroxyls. These side reactions between surface oxygen and

267 nitrogen groups might produce the formation of pyridine, pyrrole, and other nitrogen
268 functionalities [36, 45], explaining the high nitrogen content observed for pyrolyzed samples in
269 Table 1, and in accordance to XPS analyses (discussed below).

270 The chemical reduction of surface oxygen groups of GO by the amino acids is clearly observed
271 in the decrease of CO, CO_2 and total O evolution after the functionalization of GO, shown in
272 Table 2. However, functionalization with arginine delivers a stronger chemical reduction, as
273 pointed out by the larger decrease on CO_2 evolution values observed in Table 2. Figure 2c and 2d
274 shows the detailed TPD profiles (for CO and CO_2, respectively) of GO-His and GO-Arg for a
275 clearer understanding of their differences. It can be seen that stronger chemical reduction of GO
276 caused by arginine is mostly related to the removal of anhydrides and lactones, since CO_2
277 evolution at temperatures higher than 300 ºC is mostly suppressed, Figure 2.d. The slightly larger
278 CO evolution at 250-500 ºC for this sample, Figure 2.c, could be related to the decomposition of
279 the carbonyl group of the amide bridges, as previously reported in the literature [36]. Finally,
280 since the amino acids also have carboxylic functions in their structure, the CO_2 TPD profile of
281 arginine and histidine are also included in Figure 2.d for comparison purposes (dotted lines). It is
282 seen that the carboxylic acid groups of the amino acids decompose producing the release of
283 carbon dioxide at temperatures between 260 and 400 ºC. These desorption peaks are not
284 observed in the GO-His or GO-Arg profiles, which can be due to changes in the stability and
285 therefore in the thermal decomposition reactions of amino acids once they are linked to the
286 surface of GO.

287

288

3.2. Characterization of Fe-rGO-AA electrocatalysts

The chemical composition of Fe-rGO-AA electrocatalysts was determined by ultimate analyses, the results are compiled in Table 1. To evaluate the effect of the addition of iron in Fe-rGO-AA catalysts, GO-AA samples were also pyrolyzed at 800 ºC to obtain N-doped ORR catalysts (rGO-AA in Table 1). The pyrolysis of GO-AA decreases the oxygen and nitrogen contents. However, the final content of nitrogen is in the range of 2.5-5 %wt, confirming the formation of nitrogen-rich carbon materials. These amounts are lower than those reported by Wang et al. in the production of N-doped carbon nanosheets, where histidine and cysteine are pyrolyzed in the presence of zinc nitrate, achieving N contents of 8.2 and 7.6 wt. %, respectively [46]. Interestingly, sulfur doping is also attained in rGO-Cys sample, although the incorporation of nitrogen seems to be promoted over that of sulfur (N:S atomic ratio increases from 2.0 up to 3.3 after pyrolysis). A similar finding was obtained by Zhang et al. when pyrolyzing polydopamine-cysteine functionalized rGO, attaining preferential N-doping on the resulting sample [47, 48]. When pyrolysis is performed in the presence of iron species (Fe-rGO-AA samples in Table 1), a clear increase in carbon content is achieved, reaching values close to 90% for all the samples. This is an expected outcome, given that iron is a well-known graphitization catalyst [49]. Unfortunately, the presence of iron nitrate suppresses partially the high nitrogen doped levels observed in iron-free samples.

XPS analysis was used to investigate the composition and oxidation state of the synthesized samples. Table 3 collects the chemical composition (wt %) of the parent GO-AA and the derived Fe-rGO-AA catalysts. The formation of rGO is confirmed by the increase of carbon amount after the thermal treatment. The thermal reduction of surface oxygen groups is behind the decrease in O amount after pyrolysis, even though some oxygen remains forming the iron spinel detected by

312 XPS and XRD (see section 3.3). Comparison of the C1s profiles of GO, GO-His and GO-Arg,
313 Figure 3.a, confirms a stronger reduction of GO after the functionalization of GO with arginine,
314 as pointed out by the larger decrease in the band at 286.5 eV, which is related to the presence of
315 labile epoxides of GO. Similar trend can be observed in the C1s spectrum of GO-Cys, Figure S1.

Table 3. XPS composition of electrocatalysts (wt.%)

sample	C	N	O	Fe	S
Fe-rGO-Arg	76.7	2.0	12.7	8.6	0.0
Fe-rGO-Cys	85.2	2.1	6.3	5.1	1.2
Fe-rGO-His	92.4	1.3	5.5	0.9	0.0

316

317 The N-doping of r-GO is confirmed by the presence of nitrogen even after the thermal
318 pyrolysis of the GO-AA in the presence of iron nitrate, observed in Table 1. The amount of
319 nitrogen ranges from 1.3 to 2.1%, Table 3. Given the higher nitrogen content in the molecular
320 structure of arginine, the maximum N loading is achieved in Fe-rGO-Arg. In the light of the low
321 amount of nitrogen generated in Fe-rGO-His and the lower decrease in oxygen content observed
322 in ultimate analyses, it is proposed that the imidazole group in histidine is hindering both the
323 chemical reduction capacity of the amino function and its ability to form stable covalent bond
324 with the surface oxygen groups of GO during the functionalization stage.

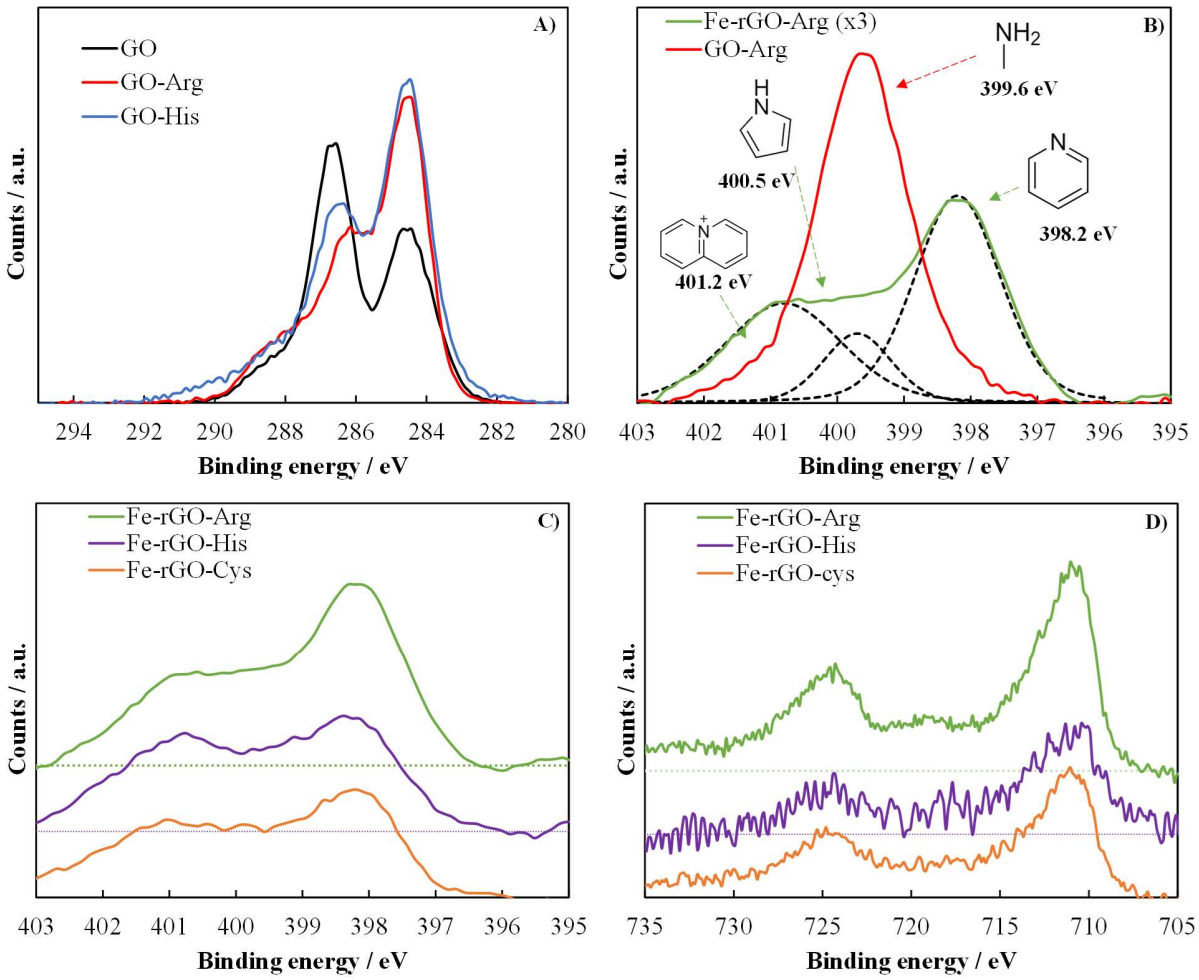

Figure 3. XPS of A) C1s region for GO, GO-His and GO-Arg, B) N1s region of GO-Arg and Fe-rGO-Arg, C) N1s and D) Fe2p region of Fe-rGO-AA electrocatalysts.

The cysteine functionalization of GO also delivers sulfur doping after the pyrolysis of the sample, with Fe-rGO-Cys showing 1.2% of S on its surface. Binding energy of 163.9 eV in the S2p peak of this sample (not shown for brevity sake) confirmed the formation of thiol groups during the pyrolysis of this sample, while the formation of metal sulfides (binding energy of 161.5 eV) can be discarded [50]. Interestingly, the amount of iron detected by XPS on the surface of rGO depends on the amino acid utilized for the functionalization. Thus, GO-Arg seems to retain the highest amount of iron, 8.6%, whereas GO-His is barely able to fix iron on its

surface. The presence of an additional available amine group on arginine, and the sulfide group in cysteine could enhance the fixation of iron, since both groups are reported to interact with iron cations [51].

The changes in the chemical speciation and oxidation state of nitrogen species between Fe-Arg and Fe-rGO-Arg are compared in Figure 3.b, revealing that the amino functional group of the parent Fe-Arg sample are incorporated after pyrolysis in Fe-rGO-Arg, mainly as pyridine groups (N-6, 55%) and quaternary nitrogen (N-Q, 30%) and also, though in lesser amounts, as pyrrole groups (N-5, 15%) [52]. The nitrogen doping of the graphene layer was also observed in the other electrocatalysts, as evidenced by the XPS profiles in the N1s region shown in Figure 3.c. However, the distribution of nitrogen functional groups is different, being slightly richer in pyridines when cysteine is used as nitrogen source (45% N-6, 30% N-Q, 25% N-Q), and richer in quaternary nitrogen for histidine (40% N-Q, 30% N-6, 30% N-5). In the case of the iron speciation, the Fe2p region revealed minor differences between the analyzed electrocatalysts, Figure 3.d. The observed peaks at 710.7 eV (Fe $2p_{3/2}$) and 724.2 eV ($2p_{1/2}$) were located at intermediate values between those expected to Fe^{3+} (711/724.8 eV) and Fe^{2+} (709/722.6 eV), and the lack of the corresponding satellite peak in the 714-718 eV region (indicative of the presence of Fe_2O_3), can be considered as an evidence of the formation of Fe_3O_4 [53], although the presence of small amount of Fe_2O_3 cannot be discarded attending solely to this technique.

Figure 4 shows the XRD patterns for Fe-rGO-Arg, Fe-rGO-His and Fe-rGO-cysteine samples. Apart from the diffraction 10 peak from the reduced graphene oxide at 43.1 º, which indicates a short range order of stacked graphene layers [54], the main crystalline peaks observed in these patterns (marked as *) are in good agreement with the reference data of the cubic spinel structure of Fe_3O_4 (JCPDS card 65-3107), as expected from the XPS results. However, the reference

pattern of γ-Fe_2O_3 (JCPDS card 39-1356) is known to share the same features, hindering the accurate identification of the crystalline phases. The 311 peak in Fe-rGO-His and Fe-rGO-Cys is located at 35.53 º, which is between that of Fe_3O_4 (35.42 º), and γ-Fe_2O_3 (35.86 º). Therefore, it is proposed that a mixture of both crystalline phases, richer in Fe_3O_4, is likely to coexist in the surface of these samples [55]. In the case of the Fe-rGO-Arg, the position is shifted to about 35.63 º and the width of the crystalline peaks are larger, probably as a consequence of a larger contribution of γ-Fe_2O_3 phase in this sample. As for the dispersion of the iron, the intensity of the peaks follows the order Arg>Cys>His. It seems like the higher iron content of Fe-rGO-Arg favors the formation of larger crystalline domains, while the functionalization with histidine enhances the dispersion of iron on the surface of the obtained electrocatalyst.

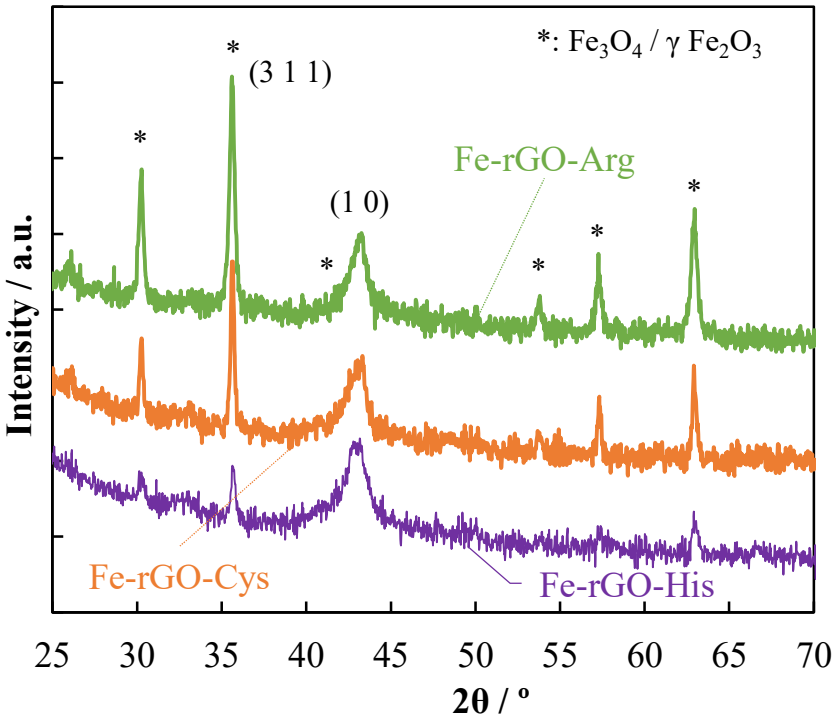

Figure 4. XRD patterns of Fe-rGO-Arg, Fe-rGO-His and Fe-rGO-Cys samples.

Raman spectroscopy was utilized to evaluate the structure of GO-AA and Fe-rGO-AA catalysts. First order Raman region is presented in Figure 5, where the peaks traditionally related to defect peak (D band) and graphitic lattice peak (G band) can be clearly seen [56]. The position of E_D and E_{2g} bands for graphite are also included as a guideline of the evolution of peak shift after functionalization and pyrolysis. The GO spectrum shows a tilted baseline owing to the high fluorescence of the sample [57], a feature that is lost after functionalization of GO with AAs due to the removal of oxygen groups, Figure 5.a. After the functionalization of graphene oxide, the G peak is shifted to lower Raman shift compared to that for GO, in agreement with previous reports regarding the structure of graphene oxide [58], which is attributed to the recovery of the hexagonal network of carbon atoms. In addition, a decrease in the FWHM of the D peak is also noticeable owing to the increase of the average size of sp_2 clusters [59]. This decrease is related to the chemical reduction of the surface oxygen groups by the amino acids, a feature already reported in the literature [39]. All these trends are magnified after the pyrolysis of GO-AA in presence of iron nitrate, Fig. 5b.

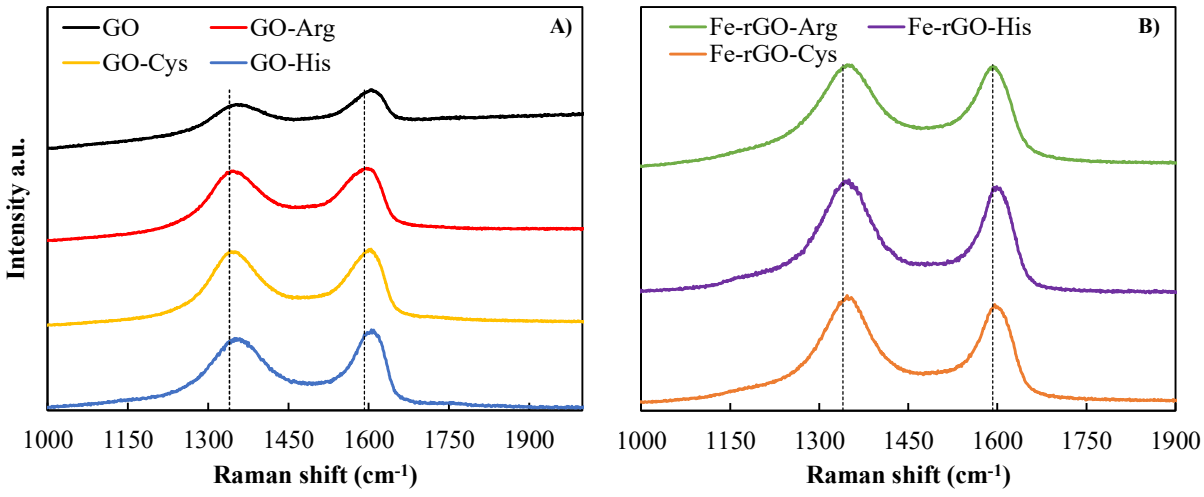

Figure 5. Raman spectra of A) GO-AA samples and b) Fe-rGO-AA electrocatalysts.

As reported by Ferrari et al., the Tuinstra-Koenig relationship between I_G/I_D and the lateral crystallite size cannot be applied in short-range ordered materials [60], explaining why this ratio decreases after the functionalization and thermal treatments of GO, in spite of the strong removal of oxygen functionalities observed by ultimate analyses, TPD and XPS. Moreover, it is difficult to spot differences between the Raman spectra of GO-AA and Fe-rGO-AA. Consequently, all the spectra were deconvoluted using 5 peaks (G, D, D', D" and D*) according to the recommendations made for the analysis of Raman spectrum of GO and rGO [58], and the most relevant parameters are compared in Table 4.

Table 4. Deconvolution parameters of Raman spectra

Sample	$F_{D''}$ / cm^{-1}	I_{D*} / %	$I_D/(I_D+I_G)$ / %
GO-Arg	183.1	1.4	81.3
GO-Cys	187.8	0.8	82.0
GO-His	160.7	1.5	84.4
Fe-rGO-Arg	140.6	4.5	71.8
Fe-rGO-Cys	137.3	3.4	72.9
Fe-rGO-His	114.3	4.4	72.0

It is seen that the narrowing of the FWMH of D" band, $F_{D''}$, is stronger in the case of histidine, followed by arginine and cysteine. According to the interpretation given by Vollebregt et al., this band is related to the presence of amorphous phase [61], and therefore functionalization with histidine seems to deliver the higher removal of disordered carbon. As expected, the Fe-rGO-His sample shows even lower values of this parameter, since the pyrolysis at 800 ºC removes preferentially the less stable amorphous carbon content. A different trend is

observed in the intensity of D* band, I_{D*}, which is related to the presence of sp_3 dangling bonds as those found in carboxyl groups and also as edges and in-plane defects [58]. The larger intensity of this band after pyrolysis can be explained due to the removal of surface oxygen groups, which generates carbon free sites at edge positions, and due to the incorporation of nitrogen groups as pyrroles, which are known to generate surface defects because of the reconstruction of the edge carbon lattice [62]. Moreover, TPD results have showed that amino acid functionalization removes carboxylic moieties, Figure 2, which is in good agreement with the low intensity value of I_{D*} obtained for GO-AA samples.

As for the lateral crystalline size, L_a, Cuesta et al. proposed the $I_D/(I_D+I_G)$ ratio as a more adequate alternative to the I_D/I_G Tuinstra-Koenig ratio for the evaluation of the Raman parameter of low structural order carbon materials [63]. Indeed, the modified $I_D/(I_D+I_G)$ ratio has been recently verified as a better descriptor of the inverse of the crystalline size in the basal plane direction, $1/L_a$, for GO and rGO [58] Table 4 shows that the values of $I_D/(I_D+I_G)$ for the GO-AA samples are very similar no matter the amino acid used (81.3-84.4%). However, the pyrolysis in the presence of iron nitrate lowers this value by an average of 10%, Table 4. The increase of the sp_2 domain sizes (e.g increase of L_a) after pyrolysis is a positive change, since it has been related to improved electrical conductivity [59], a necessary feature for electrocatalysts.

To probe the microstructure and morphology of the synthesized samples, TEM images of Fe-rGO-AA catalysts were taken at different magnifications, Figure 6. A common point in these three images is the presence of metal nanoparticles in the form of amorphous and highly dense particles on top of the wrinkle and much less dense structure of the reduced graphene oxide. The amount and agglomeration of metal particles detected at low magnification (left panel in Figure 6) is much higher for Fe-rGO-Cys and Fe-rGO-Arg, in accordance with the metal content

424 detected by XPS and the presence of crystalline phases on XRD. Conversely, smaller size
425 nanoparticles can be observed in these samples at higher magnification (right panel in Figure 6),
426 especially in the case of Fe-rGO-His. Thus, average particle size of ca. 25 nm, 30 nm and 40 nm
427 were determined for samples prepared using arginine, histidine and cysteine, respectively.

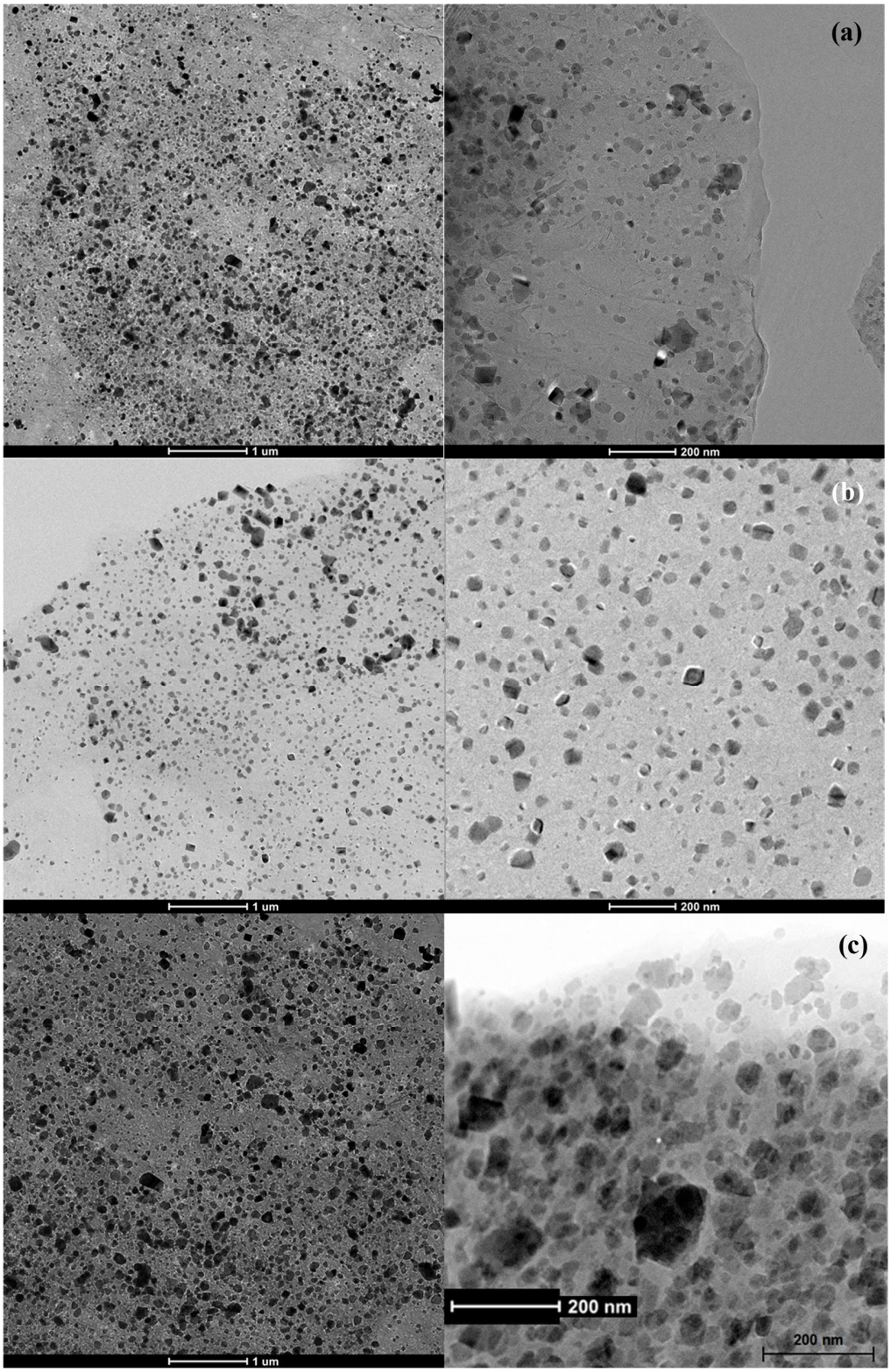

Figure 6. TEM images of (a) Fe-rGO-Arg, (b) Fe-rGO-His and (c) Fe-rGO-Cys

Likewise, elemental mapping of the samples is shown in the Fig.7. As can be seen, the flakes are mainly composed by carbon, whereas the black spots are rich in iron and oxygen, in agreement with the detection of iron oxides by XRD. Differently, nitrogen have a uniform distribution in the structure for all the samples, which is probably generated by the homogeneous functionalization of GO with AA. EDX mapping confirms that the iron distribution is greatly enhanced in Fe-rGO-His sample, showing a decreased crystalline size and the absence of massive crystalline clusters. According to these maps, it can be concluded that nitrogen incorporation into rGO, and the addition of iron to the catalysts, have been successfully obtained.

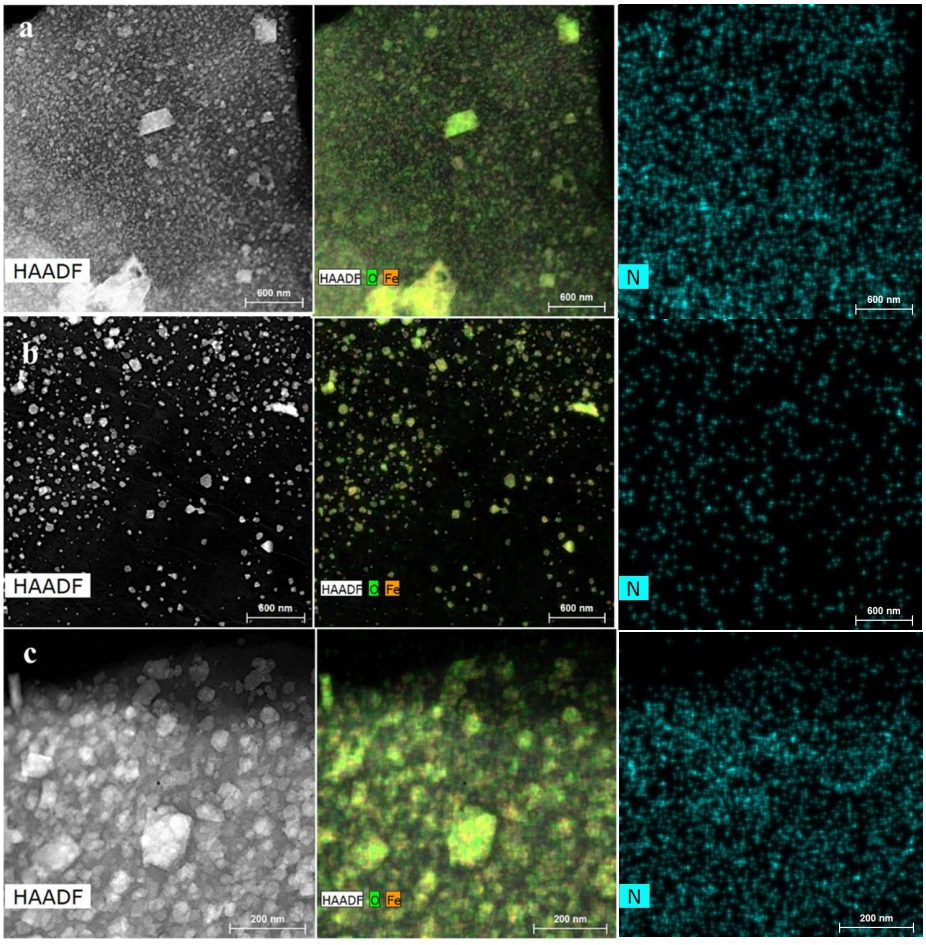

Figure 7. HAADF + EDX images of (a) Fe-rGO-Arg, (b) Fe-rGO-His and (c) Fe-rGO-Cys

3.3. Electrochemical characterization of Fe-rGO-AA electrocatalysts

Cyclic voltammetry (CV) between 0 and 1 V vs RHE of all the iron-containing samples in 0.1 M KOH were measured at 10 mV/s under inert and oxygen-saturated atmosphere using a 3-electrode cell study, and the results are shown in Fig. 8. The potential window was set in order to clarify the onset potentials of the reduction currents of oxygen reduction reaction. The CV response of all the three samples in absence of oxygen mainly presents a capacitive behavior. The negative polarization of the Fe-rGo-His and Fe-rGO-Arg electrodes gives rise to a small cathodic current at potential lower than 0.1 V, Figure 8.a. This current is probably related to the reduction processes observed in alkaline media for Fe_3O_4 electrodes, which are reported to happen around that potential value [64]. None of the other known redox features of Fe_3O_4 and Fe_2O_3 species are observed in these analyses, since they are likely to happen outside the potential limits of the CV.

The double layer capacitance of these samples was estimated from the area inside the CV recorded in inert atmosphere, obtaining values of 56 F/g for Fe-rGO-His, 22 F/g for Fe-rGO-Arg and 17 F/g for Fe-rGO-Cys. The capacitance drop in the latter samples is probably related to the massive deposition of iron oxide nanoparticles on top of the surface of rGO, disabling a large fraction of the surface area for the generation of the electric double layer. Differently, Fe-rGO-His presents not only larger capacitance, but it also shows a well-defined, box-shaped CV, pointing out the higher surface area and excellent electrical conductivity of this electrode, both valuable features for the performance of electrocatalysts. The improved conductivity is probably related to the higher structural order observed in Raman (Figure 5 and Table 4) and to the preferential N-Q doping of the sample confirmed by XPS (Figure 3), which has been reported to enhance the electrical conductivity of N-doped carbon materials [65]. Moreover, the lower

amount of iron observed in Fe-rGO-His, along with the higher double layer capacitance contribution, explain why the cathodic current of Fe_3O_4 reduction is barely seen. However, the slope of the negative scan on this electrode also increases at 0.1 V, pointing out some small contribution of the reduction of iron species observed in Fe-rGO-His sample.

Further comparison of the CVs recorded in O_2-free and O_2-saturated electrolyte are delivered in Figure 8.b-d for a better assessment of the ORR activity in these samples. In oxygen-saturated electrodes, strong and clear cathodic currents are observed in all the cases, which are undoubtedly related to the electrochemical reduction of oxygen. Nevertheless, the onset potential of oxygen reduction reaction depends on the electrocatalyst of choice, following the order Fe-rGO-His > Fe-rGO-Cys >> Fe-rGO-Arg. Thus, the catalytic activity is clearly unrelated to the amount of iron in the electrocatalysts, Table 2. A result that agrees with the studies of Lefèvre and Dodelet, who reported that Fe-N electrocatalysts prepared by pyrolysis of iron porphyrin had iron contents as low as 0.5 wt.%, showing analogous ORR activity than similar samples prepared with higher loadings [66]. In fact, the low electrical conductivity of iron oxide can explain the higher electrode resistance of Fe-rGO-Arg, as depicted by the tilted CV when compared to the square-shaped CVs recorded in N_2 atmosphere for the other electrocatalysts, Figure 8.a. Even though cathodic currents of Fe-rGO-His at medium and low potentials are the largest ones, the similar ORR onset potentials registered for Fe-rGO-His (0.88 eV) and Fe-rGO-Cys (0.86 eV) do not allow to conclude the superior performance of the former sample.

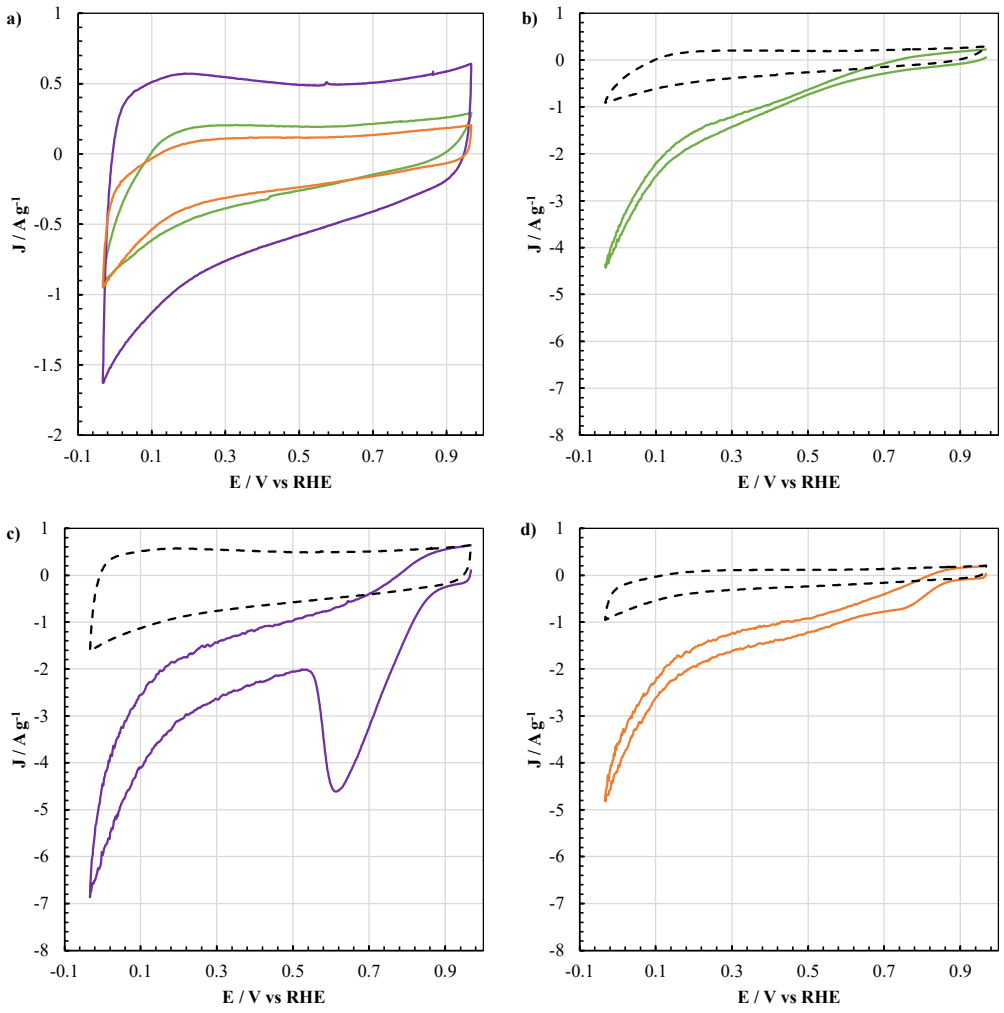

Figure 8. A) Cyclic voltametric measurements of Fe-rGO-AA samples in inert atmosphere. Comparison of CV recorded in inert (dotted lines) and oxygen saturated (solid lines) 0.1 M KOH electrolyte for B) Fe-rGO-Arg C), Fe-rGO-His and D) Fe-rGO-Cys samples.

The Rotatory Disk Electrode (RDE) assembly was used to study the ORR activity of these samples. Linear sweep voltammetry (LSV) curves at different rotation ratios were determined for all three samples and are shown in Figure 9. As expected, all the catalysts show increased ORR limiting current as rotation rate increases. However, the shape of the profile is different

493 depending on the sample. In accordance with the three-electrode cell study, Figure 8, the catalyst
494 showing the lowest activity is Fe-rGO-Arg. It shows a 2-wave profile, with the second one
495 starting at ca. 0.4 V. This feature has been ascribed to a mixed 2+2 e^- ORR mechanism [67],
496 where oxygen is reduced at high potentials to hydrogen peroxide, delivering 2 e^-, while hydrogen
497 peroxide is finally reduced to water at medium and low potentials (2^{nd} wave of the LSV profile),
498 producing the final 2 e^-. Differently, Fe-rGO-Cys and Fe-rGO-His presents only one wave,
499 reaching their diffusion limiting currents at potentials ca. 0.6 V. The I-V curve in the transition
500 region of these samples is steeper than in the case of Fe-rGO-Arg, pointing out the lower
501 resistance of these electrodes. Although the shape of the LSV profiles of the two latter samples
502 are somehow similar, Fe-rGO-His shows a higher onset potential, indicating the improved
503 catalytic activity of this electrocatalyst.
504

505

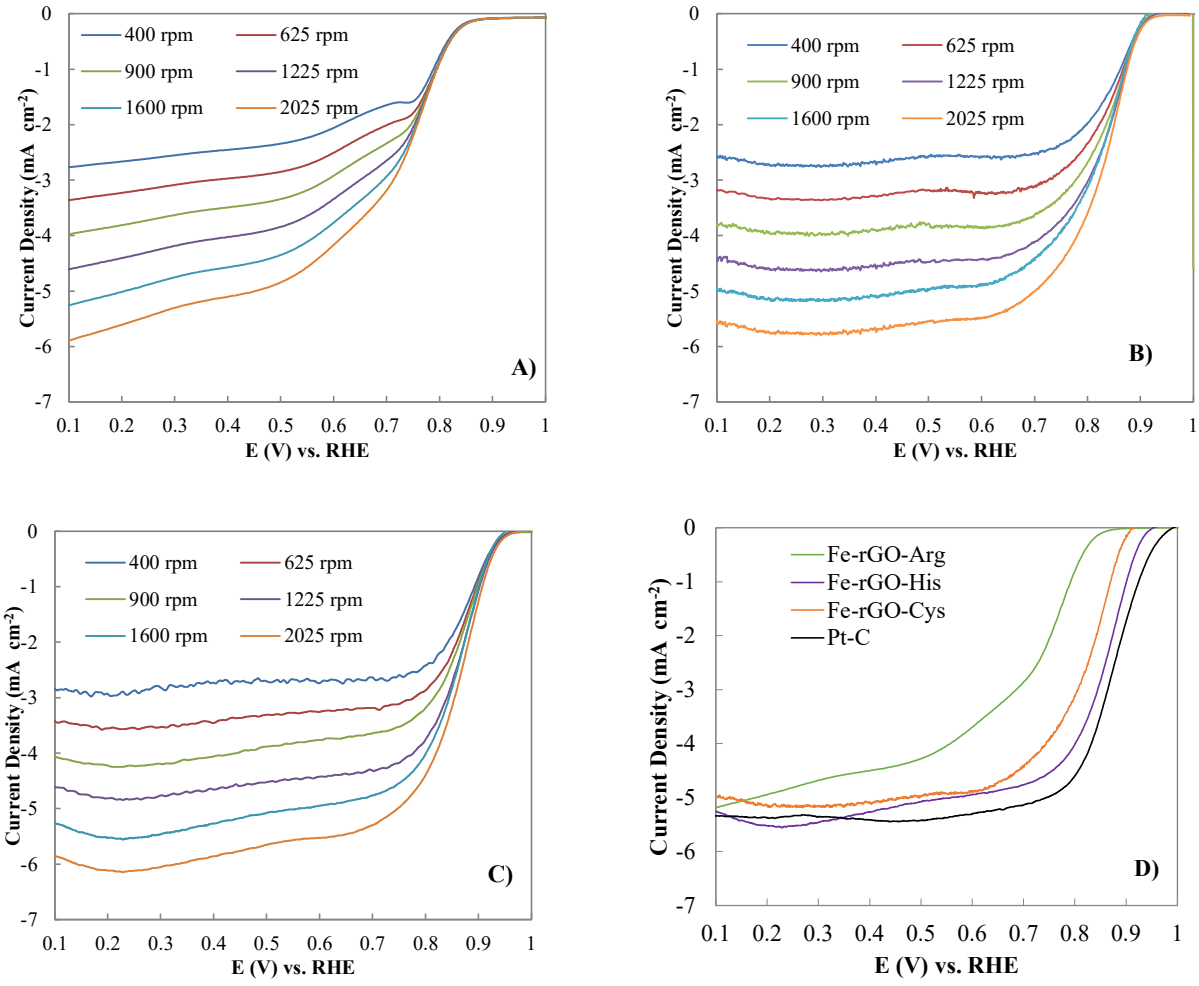

506

507 **Figure 9.** LSV curves of A) Fe-rGO-Arg, B) Fe-rGO-Cys, and C) Fe-rGO-His catalysts. D)

508 comparison between LSV profiles at 1600 rpm

509 For a clearer assessment of the activity, the LSV profiles of all the catalysts have been

510 gathered in Figure 9.d and compared with a commercial catalyst sample (20% platinum on

511 Vulcan XC72 carbon black, labelled as Pt-C). The ORR factors related to catalytic performance,

512 as the onset potential (E_0, determined at 0.1 mA/cm^2), the half wave potential ($E_{1/2}$, determined at

513 2.6 mA/cm^2 for all the samples) and the electron transfer numbers (n, calculated from the slope

514 of the KL plot as detailed in the experimental section), were determined from these LSV profiles

and compared in Table 5. Since the number of electrons is best determined by the use of a rotating ring disk electrode, the results of the KL analysis of PtC are also included for comparison purposes. It is now evident that the onset potential, a vital indicator for ORR activity, follows the order Fe-rGO-His>Fe-rGO-Cys>Fe-rGO-Arg. The superior activity of Fe-rGO-His is maintained at the half-wave potential. Moreover, the Kouteky Levich plots showed that oxygen is mainly reduced following the four-electron transfer pathway in Fe-rGO-His (n=3.94) and Fe-rGO-Cys (n=3.89), while ORR proceeds through a mixed 2+2 e^- mechanism (n=2.82) in Fe-rGO-Arg. The ORR activity of Fe-rGO-His greatly improves that achieved in metal free amino acid-doped rGO [17, 18, 30]. Even though Fe-rGO-His shows a lower amount of iron and nitrogen than the other catalysts, the lack of relationship between N and metal content has already been exposed in the literature [23, 25, 68]. To our knowledge, there are not works about the preparation of Fe-N-rGO catalysts by pyrolysis of iron salts and amino acids in the presence of GO, therefore further activity comparisons are done against Fe-N-C catalysts prepared using different supports. In this sense, activity of Fe-rGO-His is at least comparable in terms of E_{on} and $E_{1/2}$ to that of: the Fe-N-C catalysts prepared from pyrolysis of hydrothermal carbons doped with histidine and iron nitride and etched with ammonia [30]; Fe-N doped template carbons obtained by hard template method using histidine and iron (III) mixtures [28]; and doped mesoporous carbon nanostructures prepared from cysteine and porphyrins using SBA-15 as hard template [29]. Even though the commercial Pt-C catalyst still outperforms the histidine-based electrocatalyst by ca. 30 mV, Table 5, the scarcity of platinum, the low cost and high availability of iron and amino acids and the better performance in terms of resistance to cell-crossover or poisoning in Fe-N catalysts could pay off for the slightly lower activity [69, 70].

538

Table 5. ORR performance parameters

Sample	$E_{0.1}$ V	$E_{1/2}$ V	$n_{0.65}$ --
Pt-C	0.98	0.88	3.96
Fe-rGO-Cys	0.91	0.80	3.89
Fe-rGO-Arg	0.85	0.72	2.82
Fe-rGO-His	0.94	0.85	3.94

539

540 **Conclusions**

541 Graphene-based electrocatalysts were prepared by pyrolysis of graphene oxide functionalized
542 with three different amino acids, arginine, cysteine and histidine, in the presence of $Fe(NO_3)$.
543 Amino acid functionalization rendered a decrease of oxygen content due to the chemical
544 reduction of GO, following the order arginine > cysteine > histidine. The chemical reduction of
545 functionalized GO and the preferential functionalization via amide bond formation was
546 confirmed by FTIR and TPD measurements. The changes in the S:N atomic ratio for cysteine
547 and the absence of CO_2 evolution during TPD of GO-AA samples revealed that amino acids are
548 partially decomposed during the functionalization. Elemental and XPS analyses showed the
549 formation of nitrogen surface groups after the pyrolysis of GO-AA, in agreement with previous
550 results about the preparation of N-doped reduced graphene oxide following this protocol.
551 However, XPS revealed that, when iron nitrate is present during pyrolysis, the level of N-doping
552 decreases, while the carbon content and graphitization degree increased for all the obtained Fe-

553 rGO-AA samples, as observed by Raman. The combined results of XPS and XRD suggested the
554 formation of crystalline mixtures of iron spinel and iron oxide species in the catalysts, especially
555 for cysteine- and arginine-based samples, which had higher iron loadings. TEM/EDX analyses
556 also confirmed a lower amount and better dispersion of iron nanoparticles on histidine-based
557 electrocatalyst.

558 Furthermore, the electrochemical characterization in 0.1 M KOH showed that the
559 electrocatalysts prepared using cysteine and histidine delivered a larger catalytic activity for
560 ORR and an improved charge transfer, whereas the excessive fixation of iron oxide in arginine-
561 based electrocatalyst seems to be detrimental due to the negative impact in electrical resistance,
562 hindering the performance as ORR catalyst of this sample. RDE measurements revealed that Fe-
563 rGO-His was able to catalyze ORR following the desirable 4 e^- pathway, achieving onset
564 potentials only 40 mV lower than commercial platinum-based catalysts. These promising results
565 confirm that nanostructured Fe-N reduced graphene oxide catalysts with adequate ORR activity
566 can be prepared using amino acids as sustainable and low-cost precursors.

567

568 **Acknowledges**

569 The authors thank MICINN (RTI2018-097555-B-100) for financial support.

570

571 References

572 [1] Cruz-Reyes I, Trujillo-Navarrete B, García-Tapia K, Salazar-Gastélum M, Paraguay-Delgado F,
573 Félix-Navarro R. Pd/MnO2 as a bifunctional electrocatalyst for potential application in alkaline fuel cells.
574 Fuel 2020;279:118470. DOI:10.1016/j.fuel.2020.118470

575 [2] Qi J, Jin B, Liu W, Zhang W, Xu L. Converting coals into carbon-based pH-universal oxygen
576 reduction catalysts for fuel cells. Fuel 2021;285:119163. https://doi.org/10.1016/j.fuel.2020.119163

[3] Liu J, Wei L, Wang H, Lan G, Yang H, Shen J. Silk gel-based N self-doped porous activated carbon as an efficient electrocatalyst in neutral, alkaline and acidic medium. Fuel 2021;287:119485. https://doi.org/10.1016/j.fuel.2020.119485

[4] Muraoka M, Tomonaga H, Nagai M. Ammonia-treated brown coal and its activity for oxygen reduction reaction in polymer electrolyte fuel cell. Fuel 2012;97:211-8. https://doi.org/10.1016/j.fuel.2012.03.001

[5] Du W, Jiang X, Zhu L. From graphite to graphene: direct liquid-phase exfoliation of graphite to produce single-and few-layered pristine graphene. Journal of Materials Chemistry A 2013;1(36):10592-606. DOI:10.1039/C3TA12212C

[6] Bianco A, Cheng H-M, Enoki T, Gogotsi Y, Hurt RH, Koratkar N, et al. All in the graphene family–a recommended nomenclature for two-dimensional carbon materials. Elsevier; 2013. https://doi.org/10.1016/j.carbon.2013.08.038

[7] Chua CK, Pumera M. Chemical reduction of graphene oxide: a synthetic chemistry viewpoint. Chemical Society Reviews 2014;43(1):291-312. DOI:10.1039/c3cs60303b

[8] Jie W, Hao J. Graphene-based hybrid structures combined with functional materials of ferroelectrics and semiconductors. Nanoscale 2014;6(12):6346-62. https://doi.org/10.1039/C3NR06918D

[9] Mali KS, Greenwood J, Adisoejoso J, Phillipson R, De Feyter S. Nanostructuring graphene for controlled and reproducible functionalization. Nanoscale 2015;7(5):1566-85. https://doi.org/10.1039/C4NR06470D

[10] Wei J, Vo T, Inam F. Epoxy/graphene nanocomposites–processing and properties: a review. Rsc Advances 2015;5(90):73510-24. https://doi.org/10.1039/C5RA13897C

[11] Zhu Y, Murali S, Cai W, Li X, Suk JW, Potts JR, et al. Graphene and graphene oxide: synthesis, properties, and applications. Advanced materials 2010;22(35):3906-24. https://doi.org/10.1002/adma.201001068

[12] Skákalová V, Kaiser AB. Graphene: properties, preparation, characterisation and devices. Elsevier; 2014.

[13] Zhou X, Shi T, Zhou H. Hydrothermal preparation of ZnO-reduced graphene oxide hybrid with high performance in photocatalytic degradation. Applied surface science 2012;258(17):6204-11. DOI:10.1016/j.apsusc.2012.02.131

[14] Pei S, Cheng H-M. The reduction of graphene oxide. Carbon 2012;50(9):3210-28. DOI:10.1016/j.carbon.2011.11.010

[15] Ayán-Varela M, Ruiz-Rosas R, Villar-Rodil S, Paredes JI, Cazorla-Amorós D, Morallon E, et al. Efficient Pt electrocatalysts supported onto flavin mononucleotide–exfoliated pristine graphene for the methanol oxidation reaction. Electrochimica Acta 2017;231:386-95. DOI:10.1016/j.electacta.2016.12.177

[16] Sawosz E, Jaworski S, Kutwin M, Vadalasetty KP, Grodzik M, Wierzbicki M, et al. Graphene functionalized with arginine decreases the development of glioblastoma multiforme tumor in a gene-dependent manner. International journal of molecular sciences 2015;16(10):25214-33. https://doi.org/10.3390/ijms161025214

615 [17] Amiri M, Shabani AMH, Dadfarnia S, Sadjadi S. Simultaneous functionalization and reduction of
616 magnetic graphene oxide by l-histidine and its application for magnetic separation/preconcentration of
617 antioxidant trace elements. Biological trace element research 2019;190(1):262-72. DOI: 10.1007/s12011-
618 018-1545-1

619 [18] Zhang H, Niu Y, Hu W. Nitrogen/sulfur-doping of graphene with cysteine as a heteroatom source
620 for oxygen reduction electrocatalysis. Journal of colloid and interface science 2017;505:32-7.
621 https://doi.org/10.1016/j.jcis.2017.05.069

622 [19] Pan F, Duan Y, Zhang X, Zhang J. A facile synthesis of nitrogen/sulfur co-doped graphene for
623 the oxygen reduction reaction. ChemCatChem 2016;8(1):163-70. https://doi.org/10.1002/cctc.201500893

624 [20] Farmann A, Waag W, Marongiu A, Sauer DU. Critical review of on-board capacity estimation
625 techniques for lithium-ion batteries in electric and hybrid electric vehicles. Journal of Power Sources
626 2015;281:114-30. https://doi.org/10.1016/j.jpowsour.2015.01.129

627 [21] Xu P, Wu D, Wan L, Hu P, Liu R. Heteroatom doped mesoporous carbon/graphene nanosheets as
628 highly efficient electrocatalysts for oxygen reduction. Journal of colloid and interface science
629 2014;421:160-4. https://doi.org/10.1016/j.jcis.2014.02.001

630 [22] Jaouen F, Proietti E, Lefèvre M, Chenitz R, Dodelet J-P, Wu G, et al. Recent advances in non-
631 precious metal catalysis for oxygen-reduction reaction in polymer electrolyte fuel cells. Energy &
632 Environmental Science 2011;4(1):114-30. https://doi.org/10.1039/C0EE00011F

633 [23] González-Gaitán C, Ruiz-Rosas R, Morallón E, Cazorla-Amorós D. Relevance of the Interaction
634 between the M-Phthalocyanines and Carbon Nanotubes in the Electroactivity toward ORR. Langmuir
635 2017;33(43):11945-55. https://doi.org/10.1021/acs.langmuir.7b02579

636 [24] Lefèvre M, Proietti E, Jaouen F, Dodelet J-P. Iron-based catalysts with improved oxygen
637 reduction activity in polymer electrolyte fuel cells. science 2009;324(5923):71-4. DOI:
638 10.1126/science.1170051

639 [25] Ohms D, Herzog S, Franke R, Neumann V, Wiesener K, Gamburcev S, et al. Influence of metal
640 ions on the electrocatalytic oxygen reduction of carbon materials prepared from pyrolyzed
641 polyacrylonitrile. Journal of power sources 1992;38(3):327-34. https://doi.org/10.1016/0378-
642 7753(92)80122-R

643 [26] Kim D-H, Kwak D-H, Han S-B, Park H-S, Park J-Y, Won J-E, et al. The role of arginine as
644 nitrogen doping and carbon source for enhanced oxygen reduction reaction. International Journal of
645 Hydrogen Energy 2018;43(3):1479-88. https://doi.org/10.1016/j.ijhydene.2017.11.173

646 [27] Choi CH, Park SH, Woo SI. Heteroatom doped carbons prepared by the pyrolysis of bio-derived
647 amino acids as highly active catalysts for oxygen electro-reduction reactions. Green Chemistry
648 2011;13(2):406-12. https://doi.org/10.1039/C0GC00384K

649

650 [28] Kwak D-H, Han S-B, Kim D-H, Won J-E, Park K-W. Amino acid-derived non-precious catalysts
651 with excellent electrocatalytic performance and methanol tolerance in oxygen reduction reaction. Applied
652 Catalysis B: Environmental 2018;238:93-103. https://doi.org/10.1016/j.apcatb.2018.07.013

653 [29] Chen Y, Li Z, Zhu Y, Sun D, Liu X, Xu L, et al. Atomic Fe dispersed on N-doped carbon hollow
654 nanospheres for high-efficiency electrocatalytic oxygen reduction. Advanced Materials
655 2019;31(8):1806312. https://doi.org/10.1002/adma.201806312

656 [30] Wang M, Yang Y, Liu X, Pu Z, Kou Z, Zhu P, et al. The role of iron nitrides in the Fe–N–C
657 catalysis system towards the oxygen reduction reaction. Nanoscale 2017;9(22):7641-9.
658 https://doi.org/10.1039/C7NR01925D

659 [31] Marzorati S, Vasconcelos J, Ding J, Longhi M, Colavita PE. Template-free ultraspray pyrolysis
660 synthesis of N/Fe-doped carbon microspheres for oxygen reduction electrocatalysis. Journal of Materials
661 Chemistry A 2015;3(37):18920-7. https://doi.org/10.1039/C5TA02570B

662 [32] Meng C, Sheng Y, Chen Q, Tan H, Liu H. Exceptional chiral separation of amino acid modified
663 graphene oxide membranes with high-flux. Journal of Membrane Science 2017;526:25-31.
664 https://doi.org/10.1016/j.memsci.2016.12.019

665 [33] Choi W, Choi J, Bang J, Lee J-H. Layer-by-layer assembly of graphene oxide nanosheets on
666 polyamide membranes for durable reverse-osmosis applications. ACS applied materials & interfaces
667 2013;5(23):12510-9. https://doi.org/10.1021/am403790s

668 [34] Lee DW, Hong T-K, Kang D, Lee J, Heo M, Kim JY, et al. Highly controllable transparent and
669 conducting thin films using layer-by-layer assembly of oppositely charged reduced graphene oxides.
670 Journal of Materials Chemistry 2011;21(10):3438-42. https://doi.org/10.1039/C0JM02270E

671 [35] Lin L, Zhu Q, Xu A-W. Noble-metal-free Fe–N/C catalyst for highly efficient oxygen reduction
672 reaction under both alkaline and acidic conditions. Journal of the American Chemical Society
673 2014;136(31):11027-33. https://doi.org/10.1021/ja504696r

674 [36] Mostazo-López MJ, Ruiz-Rosas R, Morallón E, Cazorla-Amorós D. Nitrogen doped superporous
675 carbon prepared by a mild method. Enhancement of supercapacitor performance. international journal of
676 hydrogen energy 2016;41(43):19691-701. https://doi.org/10.1016/j.ijhydene.2016.03.091

677 [37] Luypaert J, Massart D, Vander Heyden Y. Near-infrared spectroscopy applications in
678 pharmaceutical analysis. Talanta 2007;72(3):865-83. https://doi.org/10.1016/j.talanta.2006.12.023

679 [38] Bourlinos AB, Gournis D, Petridis D, Szabó T, Szeri A, Dékány I. Graphite oxide: chemical
680 reduction to graphite and surface modification with primary aliphatic amines and amino acids. Langmuir
681 2003;19(15):6050-5. https://doi.org/10.1021/la026525h

682 [39] Tran DN, Kabiri S, Losic D. A green approach for the reduction of graphene oxide nanosheets
683 using non-aromatic amino acids. Carbon 2014;76:193-202. https://doi.org/10.1016/j.carbon.2014.04.067

[40] Figueiredo JL, Pereira M, Freitas M, Orfao J. Modification of the surface chemistry of activated carbons. carbon 1999;37(9):1379-89. https://doi.org/10.1016/S0008-6223(98)00333-9

[41] Ganguly A, Sharma S, Papakonstantinou P, Hamilton J. Probing the thermal deoxygenation of graphene oxide using high-resolution in situ X-ray-based spectroscopies. The Journal of Physical Chemistry C 2011;115(34):17009-19. https://doi.org/10.1021/jp203741y

[42] Solís-Fernández P, Rozada R, Paredes J, Villar-Rodil S, Fernández-Merino MJ, Guardia L, et al. Chemical and microscopic analysis of graphene prepared by different reduction degrees of graphene oxide. Journal of alloys and compounds 2012;536:S532-S7. https://doi.org/10.1016/j.jallcom.2012.01.102

[43] Lipatov A, Guinel MJ-F, Muratov DS, Vanyushin VO, Wilson PM, Kolmakov A, et al. Low-temperature thermal reduction of graphene oxide: In situ correlative structural, thermal desorption, and electrical transport measurements. Applied Physics Letters 2018;112(5):053103. https://doi.org/10.1063/1.4996337

[44] Ishii T, Kyotani T. Temperature programmed desorption. Materials science and engineering of carbon. Elsevier; 2016, p. 287-305. DOI:10.1016/B978-0-12-805256-3.00014-3

[45] Palomo J, Ternero-Hidalgo JJ, Rosas JM, Rodríguez-Mirasol J, Cordero T. Selective nitrogen functionalization of phosphorus-containing activated carbons. Fuel Processing Technology 2017;156:438-45. https://doi.org/10.1016/j.fuproc.2016.10.006

[46] Wang Y, Pan Y, Zhu L, Guo N, Wang R, Zhang Z, et al. Structure regulation of amino acids derived nitrogen doped porous carbon nanosheet through facile solid state assembly method. Microporous and Mesoporous Materials 2019;277:36-44. https://doi.org/10.1016/j.micromeso.2018.10.011

[47] Zhang H, Liu X, He G, Zhang X, Bao S, Hu W. Bioinspired synthesis of nitrogen/sulfur co-doped graphene as an efficient electrocatalyst for oxygen reduction reaction. Journal of Power Sources 2015;279:252-8. https://doi.org/10.1016/j.jpowsour.2015.01.016

[48] Moldoveanu S. Pyrolysis of Thiols and Sulfides. Techniques and Instrumentation in Analytical Chemistry 2010;28:345-7. https://doi.org/10.1016/S0167-9244(09)02812-1

[49] Lu A-H, Li W-C, Salabas E-L, Spliethoff B, Schüth F. Low temperature catalytic pyrolysis for the synthesis of high surface area, nanostructured graphitic carbon. Chemistry of materials 2006;18(8):2086-94. https://doi.org/10.1021/cm060135p

[50] Briggs D. Handbook of X-ray Photoelectron Spectroscopy CD Wanger, WM Riggs, LE Davis, JF Moulder and GE Muilenberg Perkin-Elmer Corp., Physical Electronics Division, Eden Prairie, Minnesota, USA, 1979. 190 pp. $195. Wiley Online Library; 1981. https://doi.org/10.1002/sia.740030412

[51] Nielsen AH, Lens P, Vollertsen J, Hvitved-Jacobsen T. Sulfide–iron interactions in domestic wastewater from a gravity sewer. Water research 2005;39(12):2747-55. DOI: 10.1016/j.watres.2005.04.048

[52] Raymundo-Piñero E, Cazorla-Amorós D, Linares-Solano A. The role of different nitrogen functional groups on the removal of SO2 from flue gases by N-doped activated carbon powders and fibres. Carbon 2003;41(10):1925-32. https://doi.org/10.1016/S0008-6223(03)00180-5

[53] Stobinski L, Lesiak B, Malolepszy A, Mazurkiewicz M, Mierzwa B, Zemek J, et al. Graphene oxide and reduced graphene oxide studied by the XRD, TEM and electron spectroscopy methods. Journal of Electron Spectroscopy and Related Phenomena 2014;195:145-54. https://doi.org/10.1016/j.elspec.2014.07.003

[54] Yamashita T, Hayes P. Analysis of XPS spectra of Fe2+ and Fe3+ ions in oxide materials. Applied surface science 2008;254(8):2441-9. https://doi.org/10.1016/j.apsusc.2007.09.063

[55] Zhang X, Niu Y, Meng X, Li Y, Zhao J. Structural evolution and characteristics of the phase transformations between α-Fe 2 O 3, Fe 3 O 4 and γ-Fe 2 O 3 nanoparticles under reducing and oxidizing atmospheres. CrystEngComm 2013;15(40):8166-72. https://doi.org/10.1039/C3CE41269E

[56] Lespade P, Marchand A, Couzi M, Cruege F. Characterization of carbon materials with Raman microspectrometry. Carbon 1984;22(4-5):375-85. DOI:10.1016/0008-6223(84)90009-5

[57] Shang J, Ma L, Li J, Ai W, Yu T, Gurzadyan GG. The origin of fluorescence from graphene oxide. Scientific reports 2012;2(1):1-8. DOI: 10.1038/srep00792

[58] Claramunt S, Varea A, Lopez-Diaz D, Velázquez MM, Cornet A, Cirera A. The importance of interbands on the interpretation of the Raman spectrum of graphene oxide. The Journal of Physical Chemistry C 2015;119(18):10123-9. https://doi.org/10.1021/acs.jpcc.5b01590

[59] Mattevi C, Eda G, Agnoli S, Miller S, Mkhoyan KA, Celik O, et al. Evolution of electrical, chemical, and structural properties of transparent and conducting chemically derived graphene thin films. Advanced Functional Materials 2009;19(16):2577-83. https://doi.org/10.1002/adfm.200900166

[60] Ferrari AC, Meyer JC, Scardaci V, Casiraghi C, Lazzeri M, Mauri F, et al. Raman spectrum of graphene and graphene layers. Physical review letters 2006;97(18):187401. DOI:10.1103/PhysRevLett.97.187401

[61] Vollebregt S, Ishihara R, Tichelaar F, Hou Y, Beenakker C. Influence of the growth temperature on the first and second-order Raman band ratios and widths of carbon nanotubes and fibers. Carbon 2012;50(10):3542-54. https://doi.org/10.1016/j.carbon.2012.03.026

[62] Quílez-Bermejo J, Morallón E, Cazorla-Amorós D. Metal-Free Heteroatom-doped Carbon-based catalysts for ORR. A critical assessment about the role of heteroatoms. Carbon 2020. https://doi.org/10.1016/j.carbon.2020.04.068

[63] Cuesta A, Dhamelincourt P, Laureyns J, Martinez-Alonso A, Tascon JM. Comparative performance of X-ray diffraction and Raman microprobe techniques for the study of carbon materials. Journal of Materials Chemistry 1998;8(12):2875-9. https://doi.org/10.1039/A805841E

[64] Monteiro J, Ivanova YA, Kovalevsky A, Ivanou D, Frade J. Reduction of magnetite to metallic iron in strong alkaline medium. Electrochimica Acta 2016;193:284-92. DOI:10.1016/j.electacta.2016.02.058

[65] Ornelas O, Sieben JM, Ruiz-Rosas R, Morallon E, Cazorla-Amorós D, Geng J, et al. On the origin of the high capacitance of nitrogen-containing carbon nanotubes in acidic and alkaline electrolytes. Chemical Communications 2014;50(77):11343-6. https://doi.org/10.1039/C4CC04876H

[66] Lefèvre M, Dodelet J-P. Fe-based catalysts for the reduction of oxygen in polymer electrolyte membrane fuel cell conditions: determination of the amount of peroxide released during electroreduction and its influence on the stability of the catalysts. Electrochimica Acta 2003;48(19):2749-60. https://doi.org/10.1016/S0013-4686(03)00393-1

[67] Gabe A, Ruiz-Rosas R, González-Gaitán C, Morallón E, Cazorla-Amorós D. Modeling of oxygen reduction reaction in porous carbon materials in alkaline medium. Effect of microporosity. Journal of Power Sources 2019;412:451-64. https://doi.org/10.1016/j.jpowsour.2018.11.075

[68] Vallejos-Burgos F, Utsumi S, Hattori Y, García X, Gordon AL, Kanoh H, et al. Pyrolyzed phthalocyanines as surrogate carbon catalysts: Initial insights into oxygen-transfer mechanisms. Fuel 2012;99:106-17. https://doi.org/10.1016/j.fuel.2012.03.055

[69] Zhang J, Li CM. Nanoporous metals: fabrication strategies and advanced electrochemical applications in catalysis, sensing and energy systems. Chemical Society Reviews 2012;41(21):7016-31. https://doi.org/10.1039/C2CS35210A

[70] Morozan A, Jousselme B, Palacin S. Low-platinum and platinum-free catalysts for the oxygen reduction reaction at fuel cell cathodes. Energy & Environmental Science 2011;4(4):1238-54. https://doi.org/10.1039/C0EE00601G